PNAS RESEARCH ARTICLE | ENGINEERING

# Exceptional enhancement of mechanical properties in high-entropy alloys via thermodynamically guided local chemical ordering

Sriswaroop Dasari[a,1], Abhishek Sharma[a,1], Chao Jiang[b], Bharat Gwalani[c,d], Wei-Chih Lin[e,f], Kai-Chi Lo[e,g], Stéphane Gorsse[f], An-Chou Yeh[e,g], Srivilliputhur G. Srinivasan[a,2], and Rajarshi Banerjee[a,2]

Edited by Huajian Gao, Nanyang Technological University, Singapore, Singapore; received July 8, 2022; accepted April 18, 2023

**Understanding the local chemical ordering propensity in random solid solutions, and tailoring its strength, can guide the design and discovery of complex, paradigm-shifting multicomponent alloys. First, we present a simple thermodynamic framework, based solely on binary enthalpies of mixing, to select optimal alloying elements to control the nature and extent of chemical ordering in high-entropy alloys (HEAs). Next, we couple high-resolution electron microscopy, atom probe tomography, hybrid Monte-Carlo, special quasirandom structures, and density functional theory calculations to demonstrate how controlled additions of Al and Ti and subsequent annealing drive chemical ordering in nearly random equiatomic face-centered cubic CoFeNi solid solution. We establish that short-range ordered domains, the precursors of long-range ordered precipitates, inform mechanical properties. Specifically, a progressively increasing local order boosts the tensile yield strengths of the parent CoFeNi alloy by a factor of four while also substantially improving ductility, which breaks the so-called strength–ductility paradox. Finally, we validate the generality of our approach by predicting and demonstrating that controlled additions of Al, which has large negative enthalpies of mixing with the constituent elements of another nearly random body-centered cubic refractory NbTaTi HEA, also introduces chemical ordering and enhances mechanical properties.**

high-entropy alloys | thermodynamics | chemical ordering

Mechanical properties of single-phase high-entropy alloys (HEAs) can be unusually enhanced than many conventional single-phase engineering alloys (1–3). Recent computational and experimental studies indicate that the atomic distribution in such solid solution HEAs may not be completely random as originally believed, but exhibit localized pockets of nonrandom distributions, also called "clustered ordering" (4). While strengthening due to such local chemical clusters has been reported in Al (5), Ni (6), Fe (7) base alloys, and more recently, in complex bulk metallic glasses (8) and HEAs (9, 10), the ability to systematically engineer its nature and extent has so far eluded us.

While the quinary CoCrFeNiMn, arguably the most extensively studied HEA, has been established as a single-phase alloy (1), local chemical ordering was recently experimentally shown, and computationally validated, in its "subset" ternary CoCrNi alloy (9, 11) Similarly, direct experimental evidence of nonrandom atomic distributions has been presented in CoCrFeNiPd (4) and CoNiV (12) HEAs. While these nonrandom atomic distributions have been correlated with enhancement in mechanical properties in CoCrNi and CoCrFeNiPd HEAs, others argue that ordering has negligible or no systematic impact on the mechanical properties (13). Furthermore, while many first-principles-based density functional theory (DFT) computations show the presence of short-range order (SRO) (4, 10, 14–16) in some HEAs, the extent and underlying causes of ordering are debatable and unclear.

We initially illustrate our thermodynamic framework by first selecting a near-random solid solution—our first example being the CoFeNi HEA. The Co–Fe, Fe–Ni, and Co–Ni binary interactions are nearly ideal with the binary enthalpy of mixing close to zero (*SI Appendix*, Fig. S1) (17). Based on this critical insight, an equiatomic face-centered cubic (FCC) CoFeNi alloy was identified as a good candidate for a truly random solid solution. Therefore, this study assumes this alloy to be a near ideal FCC solid solution. Next, we use the binary enthalpy of mixing between the potential alloying elements (Al and Ti) and the components of our alloy (Co–Fe–Ni) to identify the potential for chemically induced short-range and long-range order. Al-Co, Al-Fe, and Al-Ni binary enthalpy of mixing are large negative values indicating their strong ordering tendencies. Similar trends are observed for Ti-Co, Ti-Fe, and Ti-Ni pairs (*SI Appendix*, Fig. S1).

## Significance

While high-entropy alloys (HEAs) or complex concentrated alloys are touted as potential game changer alloys, many fundamental gaps remain in our understanding of these alloys. In particular, the local atomic distributions and their propensity for chemical ordering in HEAs have garnered much interest recently. Conceptually, our paper shows that systematic control of the nature and qualitative extent of ordering in HEAs is possible, starting from simple thermodynamic binary heats of mixing considerations and correlating that with corresponding mechanical properties. This opens the intriguing possibility that thermodynamics can provide excellent a priori guidance to explore the immense compositional space and select suitable alloying elements to discover HEAs with controlled chemical ordering, exhibiting outstanding mechanical properties.

The authors declare no competing interest.

This article is a PNAS Direct Submission.



[1]S.D. and A.S. contributed equally to this work.

[2]To whom correspondence may be addressed. Email: srinivasan.srivilliputhur@unt.edu or raj.banerjee@unt.edu.

This article contains supporting information online at https://www.pnas.org/lookup/suppl/doi:10.1073/pnas.2211787120/-/DCSupplemental.

Published May 30, 2023.

We hypothesized that controlled additions of Al and Ti to the base CoFeNi random solid solution can introduce and progressively increase the extent of local chemical ordering, thereby modifying its mechanical response. Our hypothesis was tested via detailed investigations in four different alloys—CoFeNi (33Co-33Fe-33Ni at.%), $Al_{0.25}$CoFeNi (7.6Al-30.8Co-30.8Fe-30.8Ni at.%), $Al_{0.3}$CoFeNi (9.1Al-30.3Co-30.3Fe-30.3Ni at.%), and $Al_{0.3}Ti_{0.2}$CoFeNi (8.5Al-5.7Ti-28.6Co-28.6Fe-28.6Ni at.%). The compositions were chosen such that the transition from SRO tendency to fully developed long-range order (LRO) can be examined. These alloys were first homogenized and solution treated at 1,200 °C for 5 min within the single FCC phase field and then water-quenched to room temperature. The temperature was chosen based on the pseudobinary isopleths obtained from solution thermodynamic modeling (*SI Appendix*, Fig. S1). Further details regarding the basis of selection of alloy compositions are provided in *SI Appendix*. Subsequently, our samples were carefully analyzed using atom probe tomography (APT) and transmission electron microscopy (TEM), including selected area electron diffraction patterns (SAEDP) and high-resolution-scanning TEM (HR-STEM). Lastly, the mechanical properties (tensile) of these alloys were measured and correlated with the alloy microstructures. Our results show an increase in the yield strength from 181 MPa to 800 MPa with simultaneously improvement in the ductility. Thus, by coupling simple binary enthalpy of mixing-based thermodynamic arguments, experiments, and first-principles DFT-based computations, we show that enhancement in the nature and qualitative extent of chemical ordering in HEAs correlates well with systematic increase in mechanical properties.

## Results and Discussion

Fig. 1 summarizes TEM and APT results to show that the equiatomic CoFeNi HEA is a near-random solid solution. Specifically, the SAEDP from [101] FCC zone axis (in Fig. 1*A*) and the corresponding line intensity profile along $\vec{g} = (020)$ (in Fig. 1*B*) do not show any superlattice reflection, which confirms the absence of LRO in this alloy. Also, APT reconstructions of Fe and Ni atoms (shown in Fig. 1 *C* and *D*, respectively) indicate that the homogeneous distribution of atoms and the frequency distribution plot for Ni atoms are consistent with that predicted for a truly random atomic distribution (in Fig. 1*E*). Next, we added controlled amounts of Al, a substitutional solute to this random CoFeNi alloy, to introduce a chemical ordering tendency due to the strong negative enthalpies of mixing for Al-Ni, Al-Fe, and Al-Co binary pairs.

Fig. 2 summarizes microstructural characterization of the $Al_{0.25}$CoFeNi HEA with 7.6 at.% Al. The absence of superlattice reflection in SAEDP from [101] FCC zone axis (Fig. 2*A*) confirms the lack of LRO. However, the APT results shown in Fig. 2 *B*–*D* clearly indicate a departure from the randomness seen in the equiatomic parent CoFeNi alloy. The 3D distribution of Al atoms appears to be quite uniform in this alloy as shown in Fig. 2*C*. However, the concentration profile constructed across

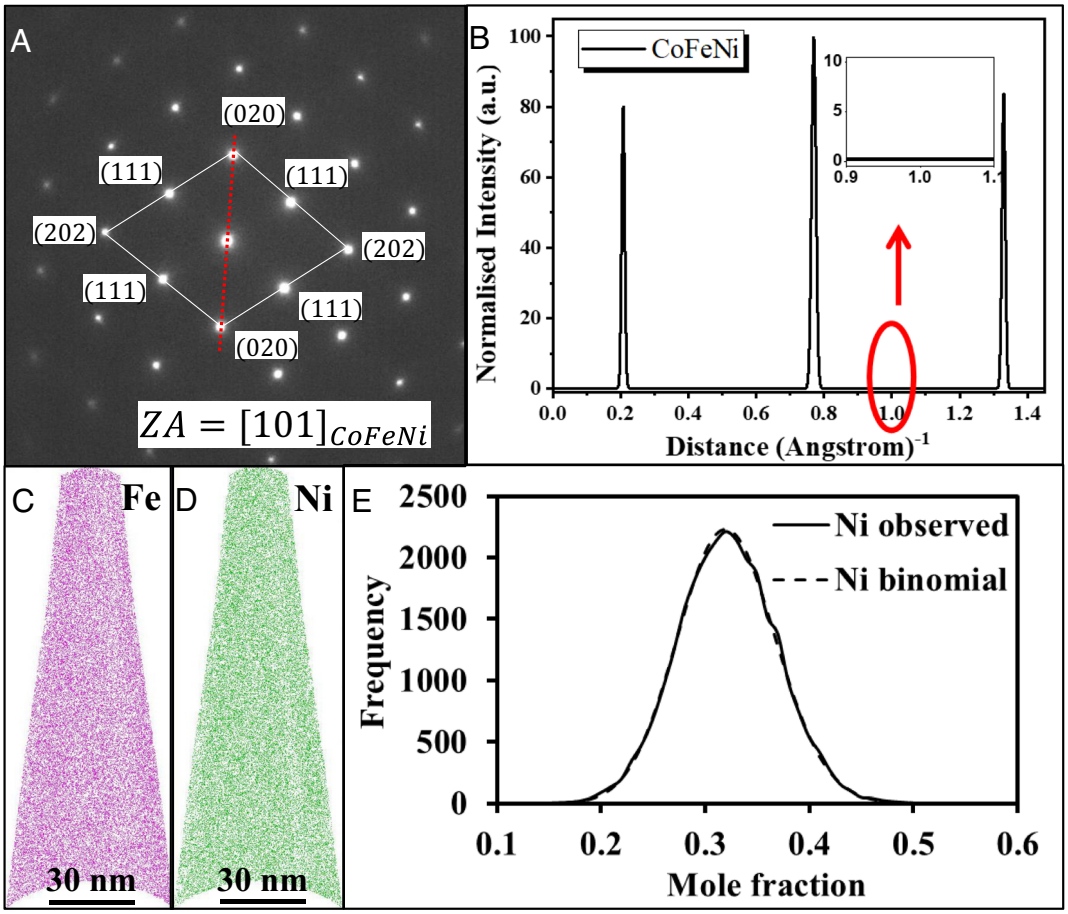


**Fig. 1.** Microstructural characterization of CoFeNi using TEM and APT. (*A*) SAEDP recorded from [101] FCC zone axis showing only fundamental reflections, indicating absence of ordering or secondary phases. (*B*) Intensity profile along the red dotted line in *A* confirms single-phase microstructure. APT ion maps of (*C*) Fe and (*D*) Ni show homogeneous distribution. (*E*) No statistically significant deviation is observed between the frequency distribution of Ni obtained from APT and the standard binomial distribution.

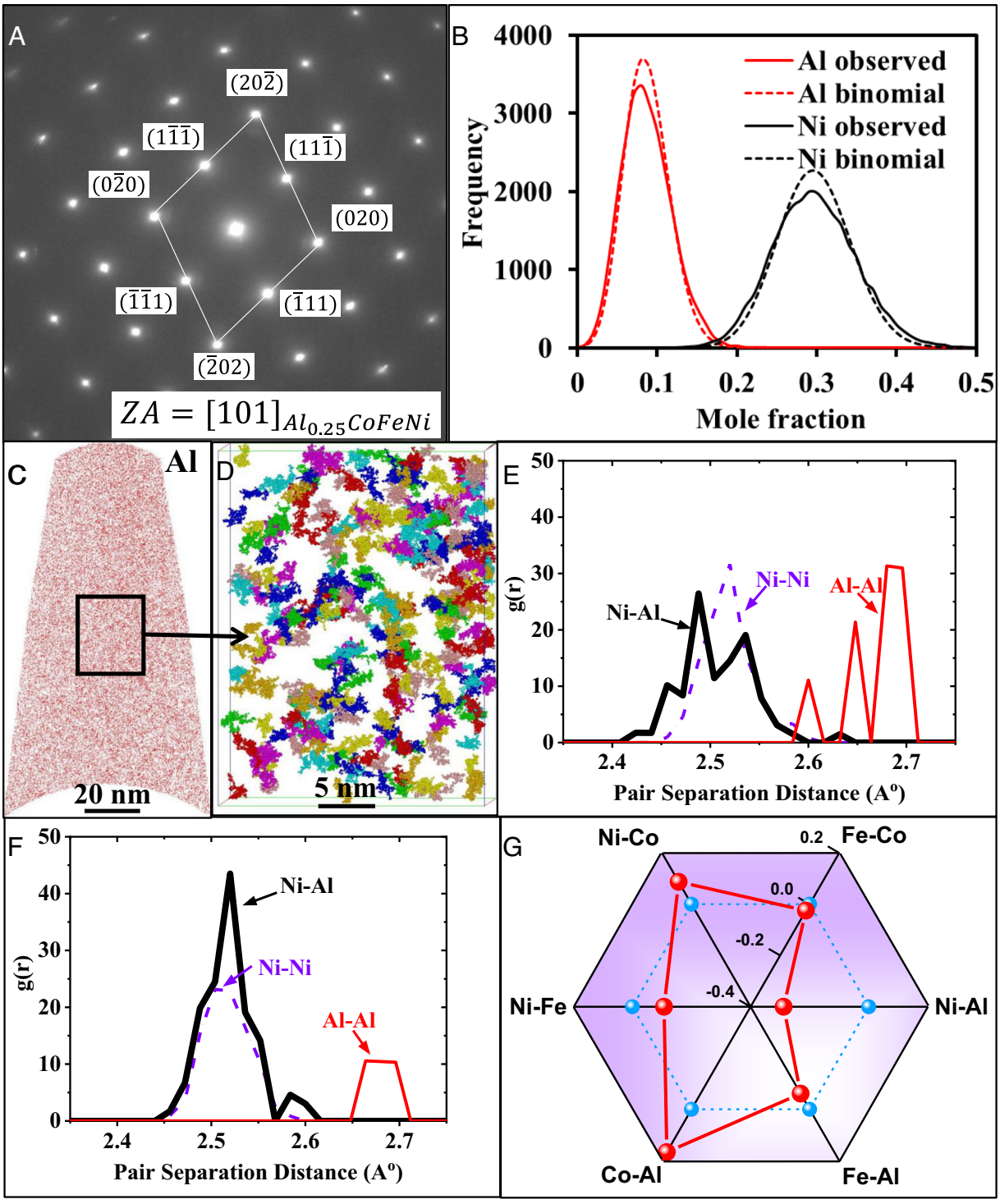


**Fig. 2.** (*A–D*) Microstructure of $Al_{0.25}$CoFeNi from TEM and APT. (*A*) SAEDP recorded from [101] FCC zone axis shows only fundamental reflections, indicating the absence of ordering or secondary phases. (*B*) Frequency distribution of Al and Ni obtained from APT when compared with binomial distributions reveals statistically significant deviations. (*C*) APT ion map of Al shows uniform distribution. (*D*) Al–Ni-rich clustered-ordering domains are revealed via cluster analysis and are colored differently. (*E*) Pair distribution functions (PDFs) of Ni–Ni, Al–Al, and Ni–Al pairs from 216-atom SQS structure for perfectly random $Al_{0.27}$CoFeNi alloy. (*F*) PDFs from 216-atom SQS structure for short-range ordered $Al_{0.27}$CoFeNi alloy annealed at 1,200 °C. (*G*) Warren–Cowley SRO parameters ($\alpha_{i\text{-}j}$) of various i and j pairs for 1NN shell. The SRO parameters for the perfectly random solid solution and the alloy with SRO at 1,200 °C are shown in sky blue and in red, respectively.

an Al 9 at.% iso-concentration surface (or isosurface) in the form of proximity histogram or proxigram (18) (shown in *SI Appendix*, Fig. S3) reveals concurrent increase of Ni and Al in some regions. Therefore, specific volume, marked by the black rectangle in Fig. 2*C*, was extracted from this 3D reconstruction and analyzed. Comparison of frequency distribution plots for Al and Ni atoms with binomial distribution (representing a random solid solution) in Fig. 2*B* indicates a departure from randomness in this alloy. Solute clustering analysis (19, 20) (detailed in methods section) of our APT data reveals Ni–Al-rich clusters with an average composition of 50Ni-15Al-18Fe-17Co at.% Al and an average diameter of 3 ± 1.5 nm (Fig. 2*D*).

The atomic scale structural details of the clusters seen in $Al_{0.25}$CoFeNi are inaccessible using APT due its limited spatial

resolution. Therefore, we performed DFT-based computations in parallel with our experimental efforts to validate the ordering seen in APT results and determine their atomic scale structure. Canonical Monte-Carlo (MC) simulations (21) probed the SRO in an FCC $Al_{0.27}$CoFeNi alloy by annealing it at 1,200 °C (identical to our experiments). Our MC simulation employs a large periodic 55296-atom supercell, constructed via a 24 × 24 × 24 extension of the conventional 4-atom FCC cubic cell. The total energy of our FCC lattice was described by summing the interaction energies between first nearest neighbor (1NN) Ni–Al, Fe–Al, Co–Al, Ni–Fe, Ni–Co, and Fe–Co pairs obtained from our DFT-calculated formation energies of $L1_2$-structured $Ni_3Al$, $Fe_3Al$, $Co_3Al$, $Ni_3Fe$, $Ni_3Co$, and $Co_3Fe$ compounds. Their values are shown in *SI Appendix*, Table S2. To overcome the prohibitive computational costs of very large supercells in DFT calculations, we generated both 108-atom and 216-atom special quasirandom structures (SQSs) (22, 23) to model the FCC $Al_{0.27}$CoFeNi alloy with SRO. As shown in *SI Appendix*, Table S3, the pair correlation functions of our SQSs agree well with those of the short-range ordered alloy predicted by our MC simulations. For comparison, SQSs for the completely random $Al_{0.27}$CoFeNi alloy were also created to closely reproduce the pair correlation functions of the random alloy (*SI Appendix*, Table S4). The pair distribution functions of the random and SRO $Al_{0.27}$CoFeNi alloy are shown in Fig. 2 *E* and *F*, respectively. Our DFT calculations with 216 (108)-atom SQSs indicate that, at 1200°C, SRO can reduce the total energy of the $Al_{0.27}$CoFeNi alloy by 0.118 (0.200) eV per Al atom. Thus, our simple 1NN bond energy model used in MC simulations remarkably predicts the energy reduction due to SRO to be 0.208 eV per Al atom, which falls in the range predicted by our DFT-SQS calculations. Importantly, such a large energy difference between the random and short-range ordered states provides a strong thermodynamic driver for ordering, which directly corroborates our experimental finding that Al additions promote SRO. From our calculated Warren–Cowley SRO parameters shown in Fig. 2*G* and *SI Appendix*, Table S5, it is evident that Ni–Al pairs dominate the short-range ordering in the $Al_3Co_{11}Fe_{11}Ni_{11}$ alloy, which agrees well with our binary enthalpies of mixing-based hypothesis. This conclusion is also consistent with the observation of the prominent first peak of Ni–Al in the PDF shown in Fig. 2*F*, confirming the presence of SRO in the $Al_{0.27}$CoFeNi alloy. Additionally, we have conducted energy-filtered TEM on CoFeNi and $Al_{0.25}$CoFeNi alloys, and these results are summarized in *SI Appendix*, Fig. S4.

Fig. 3 shows that the both the extent and nature of ordering in CoFeNi can be tuned by increasing the Al content from 7.6 at.% to 9 at.% in the $Al_{0.3}$CoFeNi HEA. The SAEDP along [101] FCC zone axis (in Fig. 3*A*) and its line intensity profile along $\vec{g} = (020)$ (in Fig. 3*B*) clearly show superlattice reflections consistent with the early stages of LRO formation. This is confirmed by the dark-field image (Fig. 3*C*) showing 3 ± 1.5 nm-sized ordered domains. Lastly, the HR-STEM micrographs shown in Fig. 3 *D*–*E*, respectively, exhibit the atomic scale structure of an LRO domain and the disordered (random solid solution) FCC matrix region. The deviation from randomness revealed in the APT frequency distribution analysis (shown in Fig. 3*F*) indicates the presence of compositionally clustered regions within the reconstruction volume. Further cluster analysis established the presence of Al–Ni-rich domains (Fig. 3*G*).

The binary thermodynamic enthalpies of mixing (*SI Appendix*, Fig. S1) indicate that Ti additions can enhance the chemical ordering tendency in CoFeNi better than Al. However, we did not investigate the $Ti_x$CoFeNi quaternary because solution thermodynamics predictions (in *SI Appendix*, Fig. S2*B*) show that Ti addition to CoFeNi beyond 7 at.% no longer maintains a single high-temperature FCC phase field, which makes it difficult to explore ordering tendencies within the solid solution. Therefore, our study adds a small amount of Ti to the $Al_{0.3}$CoFeNi alloy to expand the high-temperature single FCC phase field. The microstructural details of the resulting $Al_{0.3}Ti_{0.2}$CoFeNi HEA with 14 at% Al+Ti are summarized in Fig. 4. The strong LRO tendency in the water-quenched alloy is confirmed by the intensely sharp superlattice reflections in the SAEDP acquired along [101] FCC zone axis (Fig. 4*A*) and the corresponding line intensity profile along $\vec{g} = (020)$ shown in Fig. 4*B*. The dark-field image acquired from $\vec{g} = (1\bar{1}0)$ superlattice reflection, shown in Fig. 4*C*, reveals ~8 ± 2 nm ordered domains. HR-STEM images in Fig. 4 *D* and *E* show the LRO domains and the disordered FCC matrix, respectively. APT results from this alloy are shown in Fig. 4 *F*–*H*. The Fe ion map in Fig. 4*F* shows strong Fe enrichment in the disordered matrix within the reconstruction volume and is validated by the iso-concentration surface for Ti = 11 at.% (Fig. 4*G*). This Ti iso-concentration surface demarcates the LRO domains from the surrounding disordered FCC matrix, and Fig. 4*H* plots the compositional partitioning across the resulting interface using proxigrams (18). Additionally, the average LRO domain size visible in the dark-field image (Fig. 4*C*) agrees well with the average size of Ti-rich domains seen in APT reconstruction (Fig. 4*G*).

Collectively, these results reveal our ability to tailor the nature and extent of ordering in CoFeNi by controlled additions of Al and Ti and subsequent heat treatment. We observed a progressive increase in ordering, ranging from a near-random CoFeNi solid solution, SRO in $Al_{0.25}$CoFeNi, early-stage LRO in $Al_{0.3}$CoFeNi, and well-developed LRO in $Al_{0.3}Ti_{0.2}$CoFeNi. While the presence of LRO domains was conclusively established from additional superlattice reflections in electron diffraction and high-resolution TEM imaging, the presence of SRO domains in $Al_{0.25}$CoFeNi was established from Ni–Al-rich clusters seen in APT and from hybrid MC-, SQS-, and DFT-based calculations. The presence of these SRO domains in the case of the $Al_{0.25}$CoFeNi HEA was also inferred from the development of LRO upon isothermal annealing through thermally activated diffusion. Therefore, we next investigated the nucleation and growth of LRO domains under annealing at 500 °C from 0 to 5 h to study the effect of diffusion on ordering. *SI Appendix*, Fig. S5 shows the evolution of the Ni–Al-rich SRO domains, shown earlier in Fig. 2, into LRO domains (or precipitates) with increasing annealing times.

SAEDPs shown in *SI Appendix*, Fig. S5 *A* and *F* reveal that these LRO domains have ordered $L1_2$ crystal structure. Dark-field TEM images acquired using the $\vec{g} = (\bar{1}01)$ superlattice reflection near the [101] FCC zone axis show the presence of such $L1_2$ ordered structure within LRO domains (*SI Appendix*, Fig. S5 *B* and *G*). This was further substantiated by the filtered IFFT-HRTEM micrograph shown in *SI Appendix*, Fig. S5*C*. Alternating intensity variations from the line profile along the red dotted line shown as transparent inset in *SI Appendix*, Fig. S5*C* establish ordering. *SI Appendix*, Fig. S5*D* schematically compares $L1_2$ and FCC unit-cells. A simulated image of the {001} crystallographic plane for this $L1_2$ structure is superimposed in *SI Appendix*, Fig. S5*C* to aid interpretation. The size scale and morphology of these $L1_2$ domains agree well with the Ni–Al-rich domains delineated in the APT reconstructions using cluster analysis for the system annealed for 0.5 h (*SI Appendix*, Fig. S5*E*) and by using Al iso-concentration surfaces for the alloy annealed for 5 h (*SI Appendix*, Fig. S5*H*). Tensile stress–strain curves of alloys corresponding to these conditions, shown in *SI Appendix*, Fig. S6, reveal a progressive increase in yield strength with increasing annealing time from 0 h to 5 h without any significant change in grain size. Thus, the observed

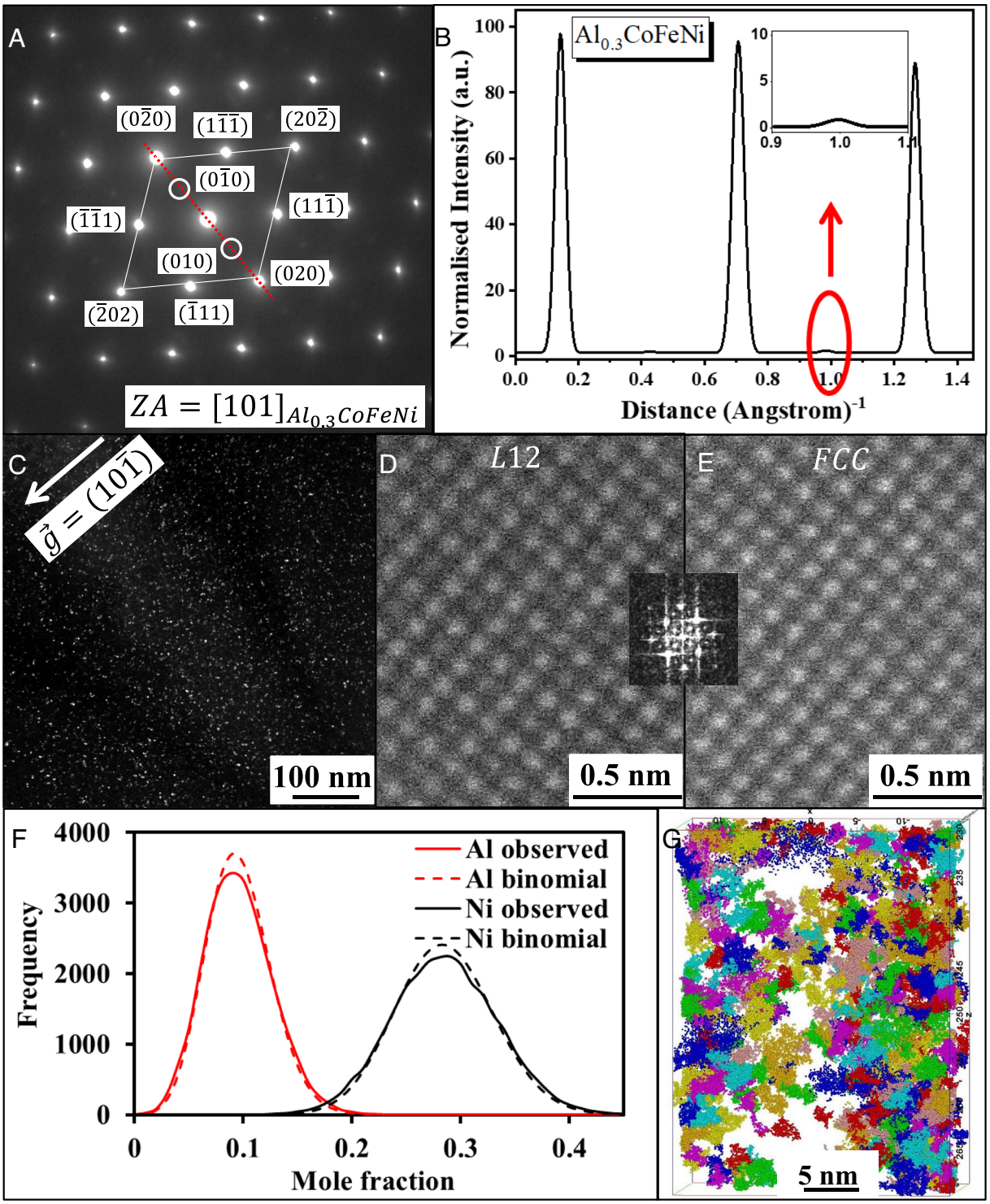


**Fig. 3.** Microstructural characterization of $Al_{0.3}CoFeNi$ using TEM and APT. (*A*) SAEDP recorded from [101] FCC zone axis shows faint superlattice reflections along with fundamental reflections, which indicate ordering. (*B*) Intensity profile along the red dotted line in (*A*) confirms ordering. (*C*) Dark-field TEM micrograph recorded from $(10\bar{1})$ reflection reveals the ordered domains. HR-STEM micrographs show ordered (*D*) and disordered (*E*) structures. (*F*) Frequency distribution of Al and Ni obtained from APT, compared with the binomial distribution, shows significant statistical deviation. (*G*) Al–Ni-rich clusters, obtained from APT.

increase in yield strength upon annealing can be attributed to the change in the extent of ordering from SRO (water-quenched at 0 h annealing) to LRO (after 0.5 h of annealing). LRO domains (or precipitates) grow upon further annealing, which substantially increases the yield strength of the HEA.

The engineering and true stress–strain plots shown in Fig. 5 *A* and *B*, respectively, show how composition-induced tuning of chemical ordering influences the room temperature tensile properties of these four HEAs, all with nominally similar grain sizes. The yield strength, tensile strength, and elongation (or tensile ductility) are summarized in Table 1. While the nearly ideal, CoFeNi random FCC solid solution has a base yield strength value of 181 MPa, the $Al_{0.25}CoFeNi$ HEA exhibiting SRO possessed a substantially higher yield strength of 287 MPa. Introduction of small (~ 3 nm) ordered domains (early-stage LRO) in $Al_{0.3}CoFeNi$ raises yield strength to 454 MPa. The introduction of well-developed LRO domains, seen in

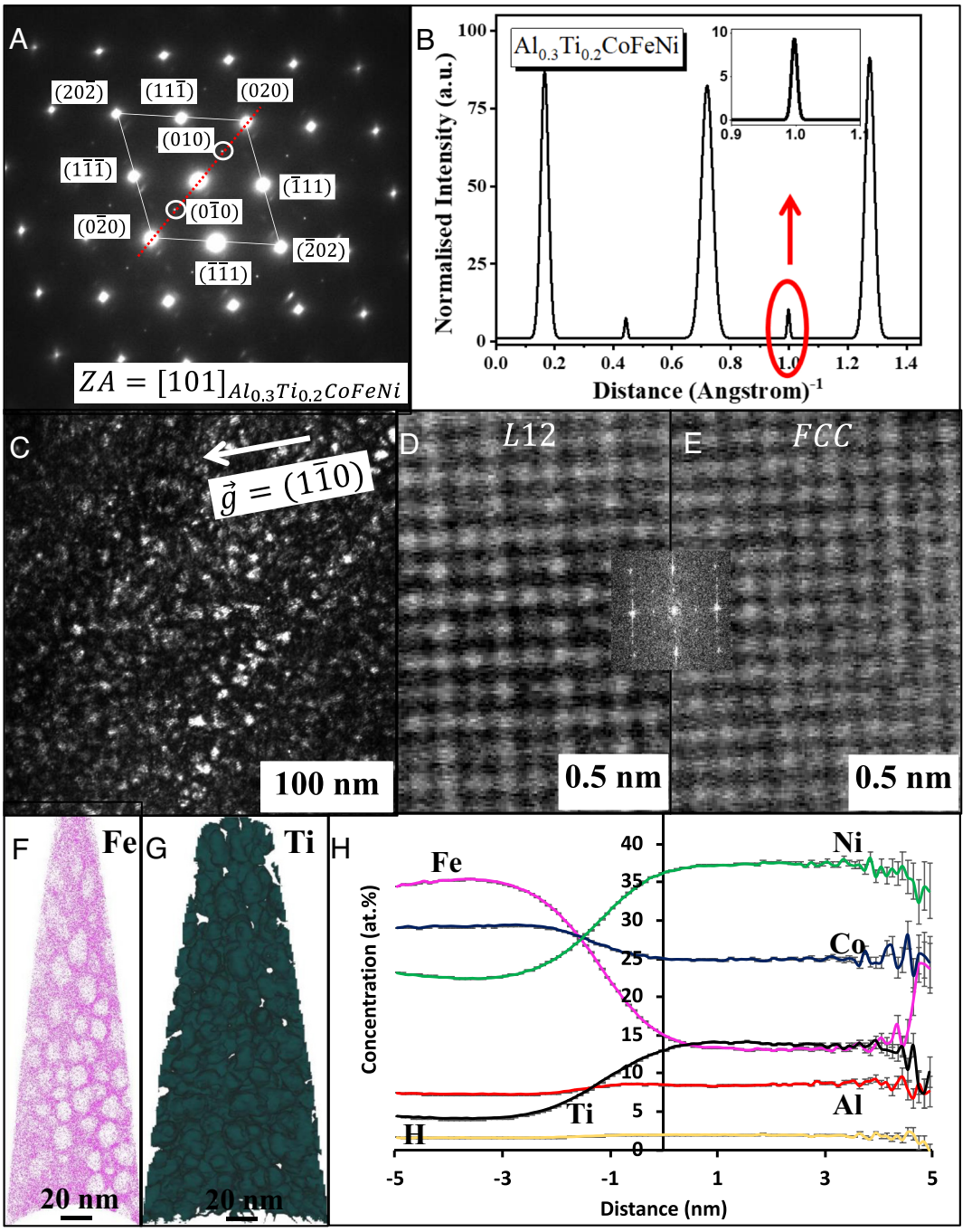


**Fig. 4.** Microstructural characterization of $Al_{0.3}Ti_{0.2}CoFeNi$ using TEM and APT. (*A*) SAEDP recorded along [101] FCC zone axis shows both sharp superlattice and fundamental reflections, indicating ordering. (*B*) Intensity profile along the red dotted line shown in *A* confirms ordering. (*C*) Dark-field TEM micrograph recorded from ($1\bar{1}0$) reflection reveals ordered domains. HR-STEM micrographs in *D* and *E* show the ordered and disordered structures, respectively. (*F* and *G*), respectively, are APT ion map of Fe, and Ti 11 at.% iso-concentration surface. The latter shows Ti-rich LRO domains. (*H*) Proximity histogram showing the elemental partitioning between FCC matrix and LRO domains. Error bars are colored gray.

$Al_{0.3}Ti_{0.2}CoFeNi$ HEA, boosts yield strength to an impressive value of 802 MPa. Corresponding increase in the ultimate tensile strengths is also observed for these alloys. Thus, the yield and tensile strengths in these HEAs progressively correlate with increasing strength of chemical order.

These HEAs also surprisingly exhibit appreciable tensile ductility values ranging from ~21% for CoFeNi to an impressive ~76% for $Al_{0.3}CoFeNi$. Thus, enhancing the extent of SRO or early stages of LRO via nanoscale ordered domains increases tensile ductility with respect to the starting near-random solid solution. Typically, a high volume fraction of ordered precipitates is well known to increase yield strength while simultaneously reducing ductility (24, 25), a bottleneck well known as the strength–ductility trade-off dilemma. The simultaneous increase in strength and ductility from CoFeNi to $Al_{0.25}CoFeNi$ to $Al_{0.3}CoFeNi$ shown here suggests that this bottleneck may be overcome by introducing ordering (SRO or early-stage LRO) within the solid solution matrix of HEAs. A recent paper reports that additions of Al, Ti, and Nb, commonly used in Ni-base superalloys, also improve strength and ductility in the CoCrNi HEA (26). However, that paper does not outline any thermodynamic basis for the choice of these elements.

Finally, to understand the deformation mechanisms our four HEAs, work-hardening rates were calculated and plotted as a function of true strain as shown in Fig. 5*C*. The work-hardening rate of

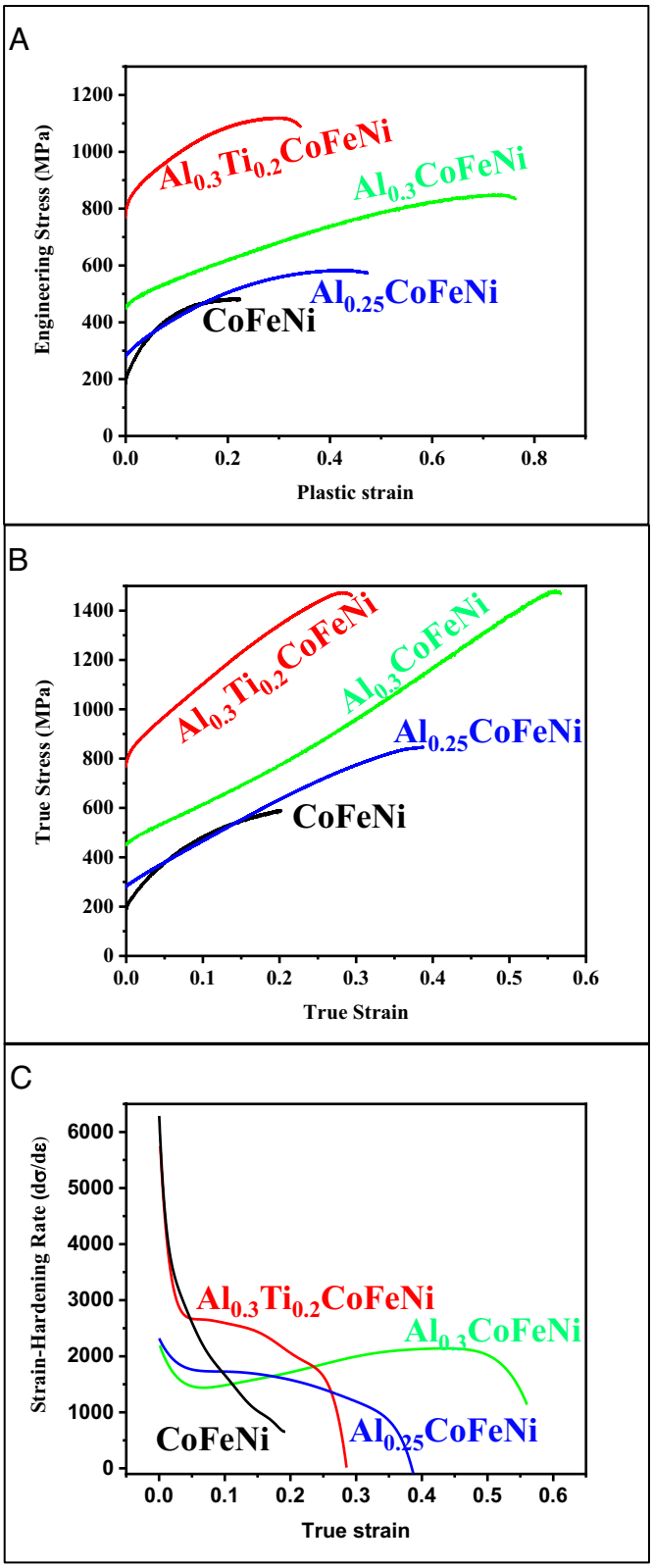


**Fig. 5.** Tensile deformation plots for CoFeNi, $Al_{0.25}$CoFeNi, $Al_{0.3}$CoFeNi, and $Al_{0.3}Ti_{0.2}$CoFeNi. (*A*) Engineering stress–strain curves. (*B*) True stress–strain curves. (*C*) Work-hardening rate plots.

equiatomic CoFeNi system constantly decreases till failure strain is reached similar to the classical work-hardening behavior seen in single-phase FCC alloys. The other HEAs with chemical ordering show a remarkable change in the work-hardening slope, indicating enhancement in ductility. We also appreciate that atomic size mismatch of Al/Ti, compared to the base CoFeNi atoms, can cause solid solution strengthening. However, the calculated solid solution strengthening effect is 20 to 30 MPa (*SI Appendix*, Table S6), indicating that the nature and extent of ordering boost tensile strengths more significantly. The predicted strengthening contributions calculated from ordered domains using coherency or precipitation strengthening models are consistent with experimentally observed yield stress values (*SI Appendix*). This further substantiates the presence of ordered domains because solid solution strengthening is unable to solely account for the observed increase in yield strength of these HEAs.

We have also performed postdeformation microscopy on CoFeNi and $Al_{0.25}$CoFeNi alloys to understand the effect of ordering on significant improvements in tensile ductility and strain hardening. These results are summarized in *SI Appendix*, Fig. S7. The SAEDP recorded from CoFeNi alloy deformed to failure ($\varepsilon_p$~ 21%) and, shown in *SI Appendix*, Fig. S7*A*, indicates no evidence of deformation-induced twinning or phase transformations during tensile testing. Furthermore, *SI Appendix*, Fig. S7*B* shows that the deformation of our CoFeNi alloy occurred via homogeneous dislocation–mediated plasticity typically observed in random FCC solid solutions. *SI Appendix*, Fig. S7*C* shows planar arrays of dislocations during early stages of plastic strain ($\varepsilon_p$~ 0.2%) in $Al_{0.25}$CoFeNi and exhibits homogeneous plasticity when deformed to failure (see planar slip bands highlighted by yellow dashed lines in *SI Appendix*, Fig. S7*D*). The postdeformation SAEDP from $Al_{0.25}$CoFeNi alloy revealing single FCC phase is shown in the inset of *SI Appendix*, Fig. S7*D*. The deformation in the alloys with ordering appears to begin with glide plane softening, which localizes the slip in multiple {111} planes. The subsequent interactions between such localized slip bands continually refine the slip length and trigger a dynamic Hall–Petch-like effect. Homogeneous dislocation–mediated plasticity subsequently sets in when a critical strain is reached within the planar slip bands, which correlates with the observed improvements in both strain hardening and elongation. This planar slip deformation mechanism is similar to the dynamic slip refinement or microband-induced plasticity observed previously (27–29). The detailed microscopy and fundamental deformation mechanisms of these alloys are subjects of future interest.

While our thermodynamics-based approach for tuning chemical ordering successfully rationalizes SRO/LRO observations in FCC-based HEAs, its general applicability requires validation. Therefore, we chose the equiatomic NbTaTi as another nearly random body-centered cubic (BCC) refractory HEA candidate because the binary enthalpies of mixing for the Nb–Ta, Nb–Ti, and Ta–Ti pairs are all nearly zero (*SI Appendix*, Fig. S1). Again, Al was selected as the alloying element to introduce chemical ordering because of its large negative enthalpies of mixing with the HEA constituent elements, Nb, Ta, and Ti (*SI Appendix*, Fig. S1). Thus, NbTaTi and $Al_{0.5}$NbTaTi HEAs were arc-melted, homogenized, solution-treated in the high-temperature (1,200 °C) single BCC phase field (*SI Appendix*, Fig. S2*D*), and quenched similar to processing route used for the FCC $Al_x$CoFeNi series of HEAs discussed above. Results from the TEM and APT analysis of the NbTaTi and $Al_{0.5}$NbTaTi HEAs are summarized in Fig. 6. The [001] BCC zone axis SAEDP from the NbTaTi alloy, shown in Fig. 6*A*, exhibits only fundamental reflections from a single BCC phase. The absence of superlattice reflections, as evidenced by the intensity profile along the g = (200) vector shown in Fig. 6*B*, establishes the lack of LRO in this alloy. Three-dimensional APT reconstructions of Ti and Nb ions in this sample (shown in Fig. 6*C*) appear nearly random. In contrast, the [001] BCC zone axis SAEDP from the $Al_{0.5}$NbTaTi alloy, shown in Fig. 6*D*, exhibits distinct superlattice reflections at the ½(200) positions, which clearly shows the presence of B2-type LRO in this HEA.

**Table. 1. Effect of the extent of ordering on the tensile properties of the four alloys**

| Alloy | Extent of ordering | Yield stress (MPa) | Ultimate tensile stress (MPa) | % elongation to failure |
|---|---|---|---|---|
| CoFeNi | No ordering | 181 ± 12 | 482 ± 6 | 21 ± 1 |
| $Al_{0.25}$CoFeNi | Short-range order revealed by APT | 287 ± 24 | 582 ± 57 | 47 ± 1 |
| $Al_{0.3}$CoFeNi | Early long-range order revealed by TEM and APT | 454 ± 22 | 853 ± 42 | 76 ± 9 |
| $Al_{0.3}Ti_{0.2}$CoFeNi | Long-range order revealed by TEM and APT | 802 ± 28 | 1121 ± 41 | 34 ± 4 |

The intensity profile along the g = (200) vector, shown in Fig. 6*E*, conclusively shows the ordering in this alloy. A TEM dark-field image, recorded using one of the superlattice reflections at the ½(200) position, shown in Fig. 6*F* reveals the nanoscale LRO domains. Early stages of clustering appear in the APT reconstructions of Ti and Al ions shown in Fig. 6*G*. Composition profiles (proximity histograms) plotted across Al = 30.4 at.% iso-concentration surfaces in the three-dimensional APT reconstruction, shown in Fig. 6*H*, reveal that the nanoscale clusters visible in Fig. 6*G* are marginally enriched in Ti and Al, while being depleted in Nb and Ta. Further, cluster analysis carried out on these APT reconstructions helped identify the location of these nanoclusters (ordered nanodomains) shown in Fig. 6*I*. The average composition of these ordered nanodomains was determined to be 23.3%Al–15.4%Nb–11.9%Ta–49.4%Ti. The average size of these clusters is 3.4 nm, in good agreement with the size of nanodomains observed in the TEM dark-field image shown in Fig. 6*F*. These results establish the success of the proposed thermodynamic design concept in introducing ordering in BCC-based refractory HEAs.

Preliminary mechanical properties of the NbTaTi and $Al_{0.5}$NbTaTi alloys have been evaluated based on compression tests and are shown in *SI Appendix*, Fig. S8. The compressive engineering stress–strain curves for the two BCC HEAs are shown in *SI Appendix*, Fig. S8*A*, revealing the nearly doubling of yield stress for the $Al_{0.5}$NbTaTi alloy (~1,039 MPa) as compared to the NbTaTi alloy (~587 MPa), while maintaining ~52% compressive plastic strain to failure. The corresponding true stress–strain and the strain-hardening curves are shown in *SI Appendix*, Fig. S8 *B* and *C*, respectively. The strain-hardening curves reveal that while the NbTaTi alloy exhibits a marginally higher strain-hardening rate during early stages of deformation, the $Al_{0.5}$NbTaTi alloy with LRO nanodomains eventually reaches higher strain-hardening rates between 10% and 40% plastic strains. The doubling of yield stress and higher strain-hardening rate in the $Al_{0.5}$NbTaTi HEA compared to the NbTaTi base alloy, while maintaining similar levels of compressive plasticity, correlates with the formation of B2-ordered nanodomains within the BCC matrix.

The binary enthalpies of mixing-based thermodynamic arguments used by us to introduce and tune local chemical ordering can also rationalize extant literature for FCC HEAs. For example, a recent observation of SRO arising due to preferential V–Co and V–Ni bonding in a ternary VCoNi alloy (12) can be explained on the basis of large negative enthalpies of mixing between V and Co/Ni. Similarly, the preferential Cr–Ni and Cr–Co bonding reported in a CoCrNi alloy is consistent with the negative binary mixing enthalpies between Cr and Ni/Co (9, 11). Yet another study attributes the heterogeneous distribution of elements in the CoCrFeNiPd HEA to the large atomic size of Pd (4). However, the high negative enthalpy of mixing between Cr and Pd could also contribute to the observed local compositional fluctuations. These alloys provide other potential prototypical systems to study and correlate the effect of ordering on the mechanical properties.

The importance of thermodynamic factors leading to local chemical ordering in HEAs is evident in the literature. To date, 32 HEA alloy systems were reported to exhibit SRO (4, 10, 15, 16, 30–53), and we could rationalize ordering tendencies in 29 alloys using the binary enthalpy of mixing-based thermodynamic principle outlined here. While we are aware of many other papers discussing enhanced mechanical properties in HEAs, our cited references focus on the influence of chemical ordering on mechanical properties. Please see including *SI Appendix*, Table S9 for more details.

Clearly, the equilibrium state of a material system, involving single or multiple phases, is dictated by the minimization of the total free energy at the temperature of interest (~1,200 °C in this study). We recognize that this results from a competition between enthalpy (favors chemical ordering or clustering) and entropy of mixing (favors chemical disordering). The effect of this competition on phase stability of HEAs has been reported in literature. For example, Otto et al. (54) used experimental and CALPHAD analysis to conclude that the entropic stabilization effect is generally insufficient to counteract the driving forces that favor the formation of secondary phases. Bokas et al. (17) reached a similar conclusion using ab-initio computations. Their analysis, based on enthalpy and entropy differences between competing solid solutions, showed that: i) the entropic driving force decreases when the number of elements increases, ii) the enthalpic contribution overall favors solid solution formation, but with a large spread due to chemistry, and iii) when combining enthalpy and entropy, adding more elements makes it statistically more difficult to form random solid solutions. Our work is consistent with these results and shows that the enthalpy of mixing can substantially impact the local ordering. Furthermore, it outlines a simple and predictive way to guide the design of HEAs by tailoring chemical ordering to tune mechanical properties.

We reiterate that our canonical MC simulations were conducted at finite temperatures and were parameterized by accurate DFT calculations. They capture SRO in our multicomponent solid solutions by fully accounting for the configurational entropy. The key conclusion from these simulations is the persistence of ordering in a fcc Ni–Fe–Co–Al alloy even at a high temperature of 1473 K. Our future studies will also include the effects of vibrational entropy to improve the accuracy of our results. Nevertheless, we argue that binary enthalpies of mixing can successfully indicate the ordering tendencies in alloys with relatively similar vibrational entropic contribution such as in our case.

*In summary*, we have proposed a general thermodynamically guided framework, validated by an integrated experimental–computational approach, to select specific alloying elements to progressively tune the nature and qualitative extent of ordering from SRO to LRO starting from near ideal random solid solution of either FCC HEA or BCC HEA. The alloying induced microstructural changes manifested as nanoscale ordered domains (or clustered ordering), which correlated well with increases in the yield and tensile strengths, and concurrent enhancement in ductility. Though some previous

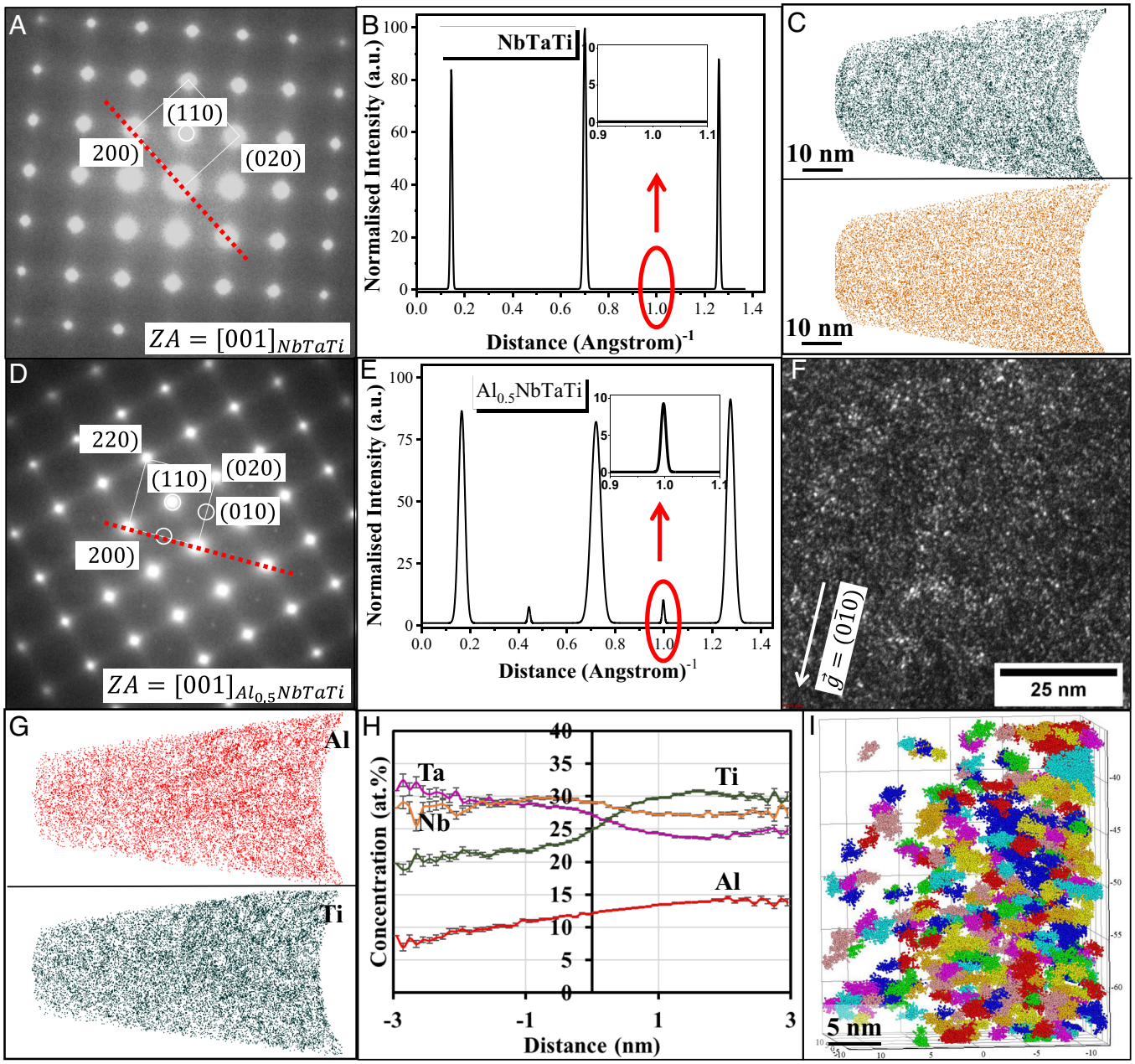


**Fig. 6.** NbTaTi and $Al_{0.5}$NbTaTi microstructural characterization using TEM and APT. (*A*) SAEDP recorded along [001] BCC zone axis showing only fundamental reflections, indicating absence of ordering and/or secondary phases. (*B*) Intensity profile along the red dotted line in *A* confirms single phase. (*C*) Ti and Nb APT ion maps show very early stages of Ti clustering. (*D*) SAEDP recorded along [001] BCC zone axis showing superlattice reflections, indicating presence of ordering. (*E*) Intensity profile along the red dotted line in *D* confirms ordering. (*F*) Dark-field TEM micrograph recorded from {001} reflection revealing the ordered domains. (*G*) APT ion map of Al and Ti showing early stages of compositional partitioning. (*H*) Proximity histogram constructed across Ti 30.4 at.% iso-concentration surface shows elemental partitioning between BCC matrix and LRO (B2) domains. Error bars are colored gray. (*I*) Al–Ti-rich clustered-ordering domains obtained from APT.

theoretical studies have rationalized chemical ordering in random solid solution HEAs, we have gone further by proposing a general thermodynamically guided hypothesis to select specific alloying elements to tune ordering, establish subsequent annealing and processing protocols to synthesize the HEAs, and use targeted experiments and computation to demonstrate the effect of tuning on mechanical properties. Significantly, our selection of alloying elements to create chemical ordering was solely guided by the thermodynamic enthalpies of mixing of constituent binary elemental pairs. This general approach, of using commonly available binary enthalpies of mixing, is broadly applicable and provides a simple and reliable map to discover HEAs with enhanced mechanical properties while starting from random base alloys. Our work demonstrates, what we believe is, a rigorous thermodynamically inspired alloy design framework and may be considered as a unique paradigm useful for developing HEAs with excellent balances of properties.

## Materials and Methods

**Material Processing.** FCC HEAs with chemical composition CoFeNi, $Al_{0.25}$CoFeNi, $Al_{0.3}$CoFeNi, and $Al_{0.3}Ti_{0.2}$CoFeNi and BCC HEAs NbTaTi and $Al_{0.5}$NbTaTi were prepared in a conventional vacuum arc melter. *SI Appendix*, Table S1 gives the nominal and measured chemical composition of these HEAs. To ensure compositionally homogeneous ingots, the alloys were flipped at least three times between consecutive rounds of melting. For FCC HEAs, the cast ingots were homogenized at a temperature of 1,200 °C for 1 h before rolling and annealing treatments. The homogenized alloys were then subjected to 50% reduction in thickness via cold

rolling and thereafter annealed at 1,200 °C for 5 min and water quenched. For BCC HEAs, the as-cast ingots alloys were directly solution treated at 1,200 °C for 48 h and water quenched.

**Microstructural Characterization.** Scanning electron microscopy (SEM) and electron backscattered diffraction (EBSD) characterization showed a texture-free polycrystalline microstructure in our HEAs. *SI Appendix*, Table S1 lists the chemical composition of all alloys, measured using X-ray energy-dispersive spectroscopy (EDS) in the SEM. Detailed characterization of the nature and extent of ordering was performed using TEM and APT.

The samples for TEM and APT were prepared away from grain boundaries using the site-specific lift-out technique on an FEI™ Nova 200 dual-beam focused ion beam (FIB) with the help of an omniprobe micromanipulator in FIB and subsequently thinned to appropriate dimensions in multiple steps by progressively reducing the voltage and/or current of the Ga ion. Crystallographic information was obtained by analyzing TEM foils using FEI Tecnai G2 TF20™ TEM operating at 200 kV. High-resolution atomic scale HAADF-STEM imaging was carried out using a Thermo-Fisher probe-corrected Themis 80 to 300 S/TEM operating at 300 kV. Energy-filtered TEM of $Al_{0.25}$CoFeNi was conducted on a Zeiss LIBRA 200MC microscope equipped with an in-column Ω energy filter at an accelerating voltage of 200 kV. Diffraction patterns were obtained in the [111] zone axis using an energy slit of 5 eV to filter inelastically scattered electrons.

APT was performed using Cameca LEAP 5000XS 3D Atom Probe Microscope operating at 30 K temperature, 0.005 to 0.01 ion/pulse detection rate in laser mode with pulse energy of 50 nJ, and 200 kHz pulse rate. IVAS 3.8.4 software was used to analyze the APT data. The mass spectrum for APT reconstructions was calibrated based on the bulk compositions obtained from SEM-EDS (*SI Appendix*, Table S1). H and Ga contamination from APT chamber and FIB was not indexed in the mass spectrum for comparing chemical composition of clustered/ordered domains with the bulk composition. The mass-to-charge ratio peaks were assigned as follows.

CoFeNi: Fe2+ (27, 28, 28.5, 29 Da), Fe+ (56 Da), Co2+ (29.5 Da), Ni2+ (29, 30, 30.5, 31, 32 Da), Ni+ (58, 60, 61, 62, 64 Da), FeH (57 Da), and NiH (59, 61, 62, 63, 65 Da). The peak overlap at 29 Da was proportionately split between Ni (major) and Fe (minor) based on natural abundance of the isotopes. Similarly, peak overlaps at 61 and 62 were appropriately split between Ni and NiH.

$Al_{0.25}$CoFeNi: Al2+ (13.5 Da), Al+ (27 Da), Fe2+ (27, 28, 28.5, 29 Da), Fe+ (56 Da), Co2+ (29.5 Da), Co+ (59 Da), Ni2+ (29, 30, 30.5, 31, 32 Da), Ni+ (58, 60, 61, 62, 64 Da), FeH (55, 57 Da), and NiH (59, 61, 62, 63, 65 Da). The peak overlaps at 27, 29, 59, 61, 63 Da were proportionately split between the relevant ions.

$Al_{0.3}$CoFeNi: Al2+ (13.5 Da), Al+ (27 Da), Fe2+ (27, 28, 28.5, 29 Da), Fe+ (54, 56, 57 Da), Co2+ (29.5 Da), Co+ (59 Da), Ni2+ (29, 30, 30.5, 31, 32 Da), Ni+ (58, 60, 61, 62, 64 Da), AlH2+ (14, 14.5 Da), FeH (55, 57 Da), and NiH (59, 61, 62, 63, 65 Da). The peak overlaps at 27, 29, 57, 59, 61, 62 Da were proportionately split between the relevant ions.

$Al_{0.3}Ti_{0.2}$CoFeNi: Al2+ (13.5 Da), Al+ (27 Da), Ti (23, 23.5, 24, 24.5, 25Da), Fe2+ (27, 28, 28.5, 29 Da), Fe+ (54, 56, 57, 58 Da), Co2+ (29.5 Da), Co+ (59 Da), Ni2+ (29, 30, 30.5, 31, 32 Da), Ni+ (58, 60, 61, 62, 64 Da), FeH (55, 57 Da), and NiH (59, 61, 62, 63, 65 Da). The peak overlaps at 27, 29, 57, 58, 59, 61, 62 Da were proportionately split between the relevant ions.

The APT data were analyzed at two length scales, first by visually examining the raw ion maps for clustered/ordered domains and second, by frequency and radial distribution analysis of select element(s) within a volume of 25 × 25 × 40 $nm^3$ exported from the original APT reconstruction. In frequency distribution analysis, the volume is divided into voxels, each containing N ions (N = 100 in this study). The mole fraction of each element in a voxel is plotted as a frequency distribution histogram. The clustering/ordering of elements can be revealed by comparing the measured distribution of the element with the theoretical binomial distribution. In contrast, radial distribution function calculates the concentration of elements as a function of radial distance from a specified center element. When the frequency or radial distribution indicated the possibility of clustering/ordering, cluster analysis is performed to uncover qualitative and quantitative details of the clusters using maximum separation method. This method consists of choosing a maximum separation distance between clustered/ordered element(s) and a minimum number of ions in the cluster based on the nearest neighbor distribution, cluster size, and cluster count distributions as detailed by Hyde et.al (19) and Stevenson et.al (20). For statistical accuracy, we performed this analysis on two different volumes for each alloy.

**Mechanical Properties.** Mechanical properties of FCC HEAs were measured at room temperature in a customized minitensile testing machine with an LVDT (linear variable displacement transformer) at a strain rate of 0.001/s. Tensile specimens with approximate gauge dimensions 5 × 1 × 1 mm were sectioned in an electric discharge machine. Three tensile specimens were tested at each condition for statistical accuracy. On the other hand, mechanical properties of our two BCC HEAs were measured via compression at a strain rate of 0.001/s at room temperature in an Instron 4,468 Universal Testing Machine. The compression samples were cylinders with ~3.6 mm diameter and 6 mm height. Two compression specimens were tested at each condition for statistical accuracy.

**DFT Calculations.** Structural relaxation and energy calculations were performed with the Vienna ab initio simulation package (VASP) (55). Spin-polarized DFT, with a plane wave energy cutoff value of 500 eV, was used. Ferromagnetic ordering was assumed in our spin-polarized calculations. Projector augmented wave potentials were employed with the Perdew–Burke–Ernzerhof generalized-gradient approximation for the exchange–correlation functional (56, 57). Brillouin zone integrations were performed using Monkhorst–Pack *k*-point meshes (58) with 5 × 5 × 5 and 5 × 5 × 3 grid, respectively, for the 108 and 216 atom systems. Finally, a conjugate-gradient algorithm was employed for structural relaxations.

**SRO Parameter for Multicomponent Alloys.** For a 1NN i–j pair in the FCC $Al_3Co_{11}Fe_{11}Ni_{11}$ alloy (i, j = Al, Co, Fe, Ni), we calculate the Warren–Cowley (59) SRO parameters $\alpha_{i\text{-}j}$ as:

$$\alpha_{i-j} = 1 - \frac{f_{i-j}}{x_i x_j} \qquad [1]$$

where $f_{i\text{-}j}$ is the fraction of 1NN i–j bonds in the alloy, and $x_i$ and $x_j$ are the mole fractions of i and j atoms, respectively. For completely random alloys, we have $\alpha_{i\text{-}j} = 0$. When $\alpha_{i\text{-}j} < 0$, there is a tendency for unlike i–j pairs as nearest neighbors compared to the random case. Lastly, $\alpha_{i\text{-}j} > 0$ indicates a tendency to cluster.

**Data, Materials, and Software Availability.** All study data are included in the article and/or *SI Appendix*.

**ACKNOWLEDGMENTS.** The work was supported by the US Air Force Office of Scientific Research grants FA9550-17-1-0395 and FA9550-20-1-0169. We acknowledge the Materials Research Facility at the University of North Texas and Center for Electron Microscopy and Analysis at The Ohio State University for use of microscopy facilities. We also kindly acknowledge Dr. Mingwei Zhang and Prof. Andrew Minor for the EFTEM work done at Molecular Foundry, which is supported by the Office of Science, Office of Basic Energy Sciences, of the U.S. Department of Energy under Contract No. DE-AC02-05CH11231. We would also like to acknowledge Talon3 High-Performance Computer Cluster at the University of North Texas and an allocation on Lonestar6 computer at Texas Academic Computing Center at Austin for modeling facilities. W.-C.L., K.-C.L., and A.-C.Y. would like to acknowledge the financial support by the "High-Entropy Materials Centre" from The Featured Areas Research Centre Program within the framework of the Higher Education Sprout Project by the Ministry of Education and from the Projects MOST110-2634-F-007-024, MOST110-2224-E-007-001, and MOST110-2221-E-007-020-MY3 by the Ministry of Science and Technology (MOST) in Taiwan.

Author affiliations: [a]Department of Materials Science & Engineering, University of North Texas, Denton, TX 76207; [b]Computational Mechanics & Materials Department, Idaho National Laboratory, Idaho Falls, ID 83415; [c]Physical and Computational Directorate, Pacific Northwest National Laboratory, Richland, WA 99354; [d]Department of Materials Science and Engineering, North Carolina State University, Raleigh, NC 27695; [e]Department of Materials Science and Engineering, National Tsing Hua University, Hsinchu 30013, Taiwan, R. O. C; [f]University Bordeaux, CNRS, Bordeaux INP, ICMCB, UMR 5026, F-33600 Pessac, France; and [g]High Entropy Materials Center, National Tsing Hua University, Hsinchu 30013, Taiwan, R. O. C

Author contributions: B.G., A.-C.Y., S.G.S., and R.B. designed research; S.D., A.S., C.J., W.-C.L., K.-C.L., S.G., and S.G.S. performed research; S.D., A.S., C.J., B.G., W.-C.L., K.-C.L., S.G., A.-C.Y., S.G.S., and R.B. analyzed data; and S.D., A.S., C.J., B.G., S.G.S., and R.B. wrote the paper.

1. G. Laplanche *et al.*, Temperature dependencies of the elastic moduli and thermal expansion coefficient of an equiatomic, single-phase CoCrFeMnNi high-entropy alloy. *J. Alloys Compd.* **623**, 348–353 (2015).
2. R. Kozak, A. Sologubenko, W. Steurer, Single-phase high-entropy alloys - An overview. *Zeitschrift fur Krist.* **230** (2015), 10.1515/zkri-2014-1739.
3. J. W. Yeh *et al.*, Nanostructured high-entropy alloys with multiple principal elements: Novel alloy design concepts and outcomes. *Adv. Eng. Mater.* **6**, 299–303 (2004).
4. Q. Ding *et al.*, Tuning element distribution, structure and properties by composition in high-entropy alloys. *Nature* **574**, 223–227 (2019).
5. A. de Vaucorbeil, C. W. Sinclair, W. J. Poole, Atomistic insights into cluster strengthening in aluminum alloys. *Materialia* **4**, 566–574 (2018), 10.1016/j.mtla.2018.11.020.
6. Y. J. Zhang, D. Han, X. W. Li, Impact of short range ordering on the anomalous four-stage strain hardening behavior of low solid-solution hardening Ni–Cr alloys. *Mater. Sci. Eng. A* **814**, 141193 (2021), 10.1016/j.msea.2021.141193.
7. Z. Xiong, I. Timokhina, E. Pereloma, Clustering, nano-scale precipitation and strengthening of steels. *Prog. Mater. Sci.* **118**, 100764 (2021), 10.1016/j.pmatsci.2020.100764.
8. J. Eckert, J. Das, S. Pauly, C. Duhamel, Mechanical properties of bulk metallic glasses and composites. *J. Mater. Res.*, 10.1557/jmr.2007.0050 (2007).
9. R. Zhang *et al.*, Short-range order and its impact on the CrCoNi medium-entropy alloy. *Nature* **581**, 283–287 (2020).
10. E. Antillon, C. Woodward, S. I. Rao, B. Akdim, T. A. Parthasarathy, Chemical short range order strengthening in a model FCC high entropy alloy. *Acta Mater.* **190**, 29–42 (2020).
11. J. Ding, Q. Yu, M. Asta, R. O. Ritchie, Tunable stacking fault energies by tailoring local chemical order in CrCoNi medium-entropy alloys. *Proc. Natl. Acad. Sci. U.S.A.* **115**, 8919–8924 (2018).
12. X. Chen *et al.*, Direct observation of chemical short-range order in a medium-entropy alloy. *Nature* **592**, 712–716 (2021).
13. B. Yin, S. Yoshida, N. Tsuji, W. A. Curtin, Yield strength and misfit volumes of NiCoCr and implications for short-range-order. *Nat. Commun.* **11**, 2507 (2020).
14. Q. J. Li, H. Sheng, E. Ma, Strengthening in multi-principal element alloys with local-chemical-order roughened dislocation pathways. *Nat. Commun.* **10**, 3563 (2019).
15. P. Singh, A. V. Smirnov, D. D. Johnson, Atomic short-range order and incipient long-range order in high-entropy alloys. *Phys. Rev. B Condens. Matter Mater. Phys.* **91**, 224204 (2015).
16. A. Fernández-Caballero, J. S. Wróbel, P. M. Mummery, D. Nguyen-Manh, Short-range order in high entropy alloys: Theoretical formulation and application to Mo-Nb-Ta-V-W system. *J. Phase Equilibria Diffus.* **38**, 391–403 (2017).
17. G. B. Bokas *et al.*, Unveiling the thermodynamic driving forces for high entropy alloys formation through big data ab initio analysis. *Scr. Mater.* **202**, 114000 (2021), 10.1016/j.scriptamat.2021.114000.
18. O. C. Hellman, J. A. Vandenbroucke, J. Rüsing, D. Isheim, D. N. Seidman, Analysis of three-dimensional atom-probe data by the proximity histogram. *Microsc. Microanal.* **6**, 437–444 (2000).
19. J. M. Hyde, E. A. Marquis, K. B. Wilford, T. J. Williams, A sensitivity analysis of the maximum separation method for the characterisation of solute clusters. *Ultramicroscopy* **111**, 440–447 (2011).
20. L. T. Stephenson, M. P. Moody, P. V. Liddicoat, S. P. Ringer, New techniques for the analysis of fine-scaled clustering phenomena within Atom Probe Tomography (APT) data. *Microsc. Microanal.* **13**, 448–463 (2007).
21. A. O. Mekhrabov, M. V. Akdeniz, Modelling and monte carlo simulation of the atomic ordering processes in Ni3Al intermetallics. *Model. Simul. Mater. Sci. Eng.* **15**, 1–12 (2007).
22. C. Jiang, First-principles study of ternary bcc alloys using special quasi-random structures. *Acta Mater.* **57**, 4716–4726 (2009).
23. A. Zunger, S. H. Wei, L. G. Ferreira, J. E. Bernard, Special quasirandom structures. *Phys. Rev. Lett.* **65**, 353–356 (1990).
24. B. Gwalani *et al.*, Tensile yield strength of a single bulk Al0.3CoCrFeNi high entropy alloy can be tuned from 160 MPa to 1800 MPa. *Scr. Mater.* **162**, 18–23 (2019).
25. J. Y. He *et al.*, A precipitation-hardened high-entropy alloy with outstanding tensile properties. *Acta Mater.* **102**, 187–196 (2016).
26. J. Miao *et al.*, Ordering effects on deformation substructures and strain hardening behavior of a crconi based medium entropy alloy. *Acta Mater.* **210**, 116829 (2021).
27. J. D. Yoo, S. W. Hwang, K. T. Park, Origin of extended tensile ductility of a Fe-28Mn-10Al-1C steel. *Metall. Mater. Trans. A Phys. Metall. Mater. Sci.* **40**, 1520–1523 (2009), 10.1007/s11661-009-9862-9.
28. E. Welsch *et al.*, Strain hardening by dynamic slip band refinement in a high-Mn lightweight steel. *Acta Mater.* **116**, 188–199 (2016), 10.1016/j.actamat.2016.06.037.
29. T. Yang *et al.*, Multicomponent intermetallic nanoparticles and superb mechanical behaviors of complex alloys. *Science* **362**, 933–937 (2018).
30. P. Singh, A. V. Smirnov, D. D. Johnson, Ta-Nb-Mo-W refractory high-entropy alloys: Anomalous ordering behavior and its intriguing electronic origin. *Phys. Rev. Mater.* **2**, 055004 (2018), 10.1103/PhysRevMaterials.2.055004.
31. S. Yin, J. Ding, M. Asta, R. O. Ritchie, Ab initio modeling of the energy landscape for screw dislocations in body-centered cubic high-entropy alloys. *npj Comput. Mater.* **6**, 1–11 (2020).
32. A. Sharma, P. Singh, D. D. Johnson, P. K. Liaw, G. Balasubramanian, Atomistic clustering-ordering and high-strain deformation of an Al0.1 CrCoFeNi high-entropy alloy. *Sci. Rep.* **6**, 31028 (2016), 10.1038/srep31028.
33. Y. Ma *et al.*, Chemical short-range orders and the induced structural transition in high-entropy alloys. *Scr. Mater.* **144**, 64–68 (2018), 10.1016/j.scriptamat.2017.09.049.
34. S. D. Wang *et al.*, Chemical short-range ordering and its strengthening effect in refractory high-entropy alloys. *Phys. Rev. B*, **103**, 104107 (2021), 10.1103/PhysRevB.103.104107.
35. S. Chen *et al.*, Simultaneously enhancing the ultimate strength and ductility of high-entropy alloys via short-range ordering. *Nat. Commun.* **12**, 4953 (2021), 10.1038/s41467-021-25264-5.
36. V. Sorkin *et al.*, First-principles-based high-throughput computation for high entropy alloys with short range order. *J. Alloys Compd.* **882**, 160776 (2021), 10.1016/j.jallcom.2021.160776.
37. F. Körmann, T. Kostiuchenko, A. Shapeev, J. Neugebauer, B2 ordering in body-centered-cubic AlNbTiV refractory high-entropy alloys. *Phys. Rev. Mater.* **5**, 053803 (2021), 10.1103/PhysRevMaterials.5.053803.
38. P. Singh, A. V. Smirnov, A. Alam, D. D. Johnson, First-principles prediction of incipient order in arbitrary high-entropy alloys: Exemplified in Ti0.25CrFeNiAlx. *Acta Mater.* **189**, 248–254 (2020), 10.1016/j.actamat.2020.02.063.
39. Q. F. He *et al.*, Understanding chemical short-range ordering/demixing coupled with lattice distortion in solid solution high entropy alloys. *Acta Mater.* **216**, 117140 (2021), 10.1016/j.actamat.2021.117140.
40. X. Huang *et al.*, Atomistic simulation of chemical short-range order in HfNbTaZr high entropy alloy based on a newly-developed interatomic potential. *Mater. Des.* **202**, 109560 (2021), 10.1016/j.matdes.2021.109560.
41. B. Zhang, J. Ding, E. Ma, Chemical short-range order in body-centered-cubic TiZrHfNb high-entropy alloys. *Appl. Phys. Lett.* **119**, 201908 (2021), 10.1063/5.0069417.
42. W. Feng, Y. Qi, S. Wang, Effects of short-range order on the magnetic and mechanical properties of FeCoNi(AlSi)x high entropy alloys. *Metals* **7**, 482 (2017), 10.3390/met7110482.
43. D. Sobieraj *et al.*, Chemical short-range order in derivative Cr-Ta-Ti-V-W high entropy alloys from the first-principles thermodynamic study. *Phys. Chem. Chem. Phys.* **22**, 23929–23951 (2020), 10.1039/d0cp03764h.
44. D. Liu *et al.*, Chemical short-range order in Fe50Mn30Co10Cr10 high-entropy alloy. *Mater. Today Nano* **16**, 100139 (2021).
45. Y. Ma *et al.*, Pressure-induced ordering phase transition in high-entropy alloy. *Intermetallics* **103**, 63–66 (2018), 10.1016/j.intermet.2018.10.003.
46. W. Z. Ding Jun, Local chemical order in high-entropy alloys. *Acta Met. Sin* **57**, 413–424 (2021).
47. W. R. Jian *et al.*, Effects of lattice distortion and chemical short-range order on the mechanisms of deformation in medium entropy alloy CoCrNi. *Acta Mater.* **199**, 352–369 (2020), 10.1016/j.actamat.2020.08.044.
48. A. Jagetia *et al.*, Ordering-mediated local nano-clustering results in unusually large hall-petch strengthening coefficients in high entropy alloys. *Mater. Res. Lett. Under Rev.* **9**, 213–222 (2020).
49. S. Guo, Y. Zhang, H. Chen, X. Li, M. Wang, Impact of local chemical order on the structure evolution of dual-phase high-entropy alloy during solidification process. *Vacuum* **18**, 109953 (2021), 10.1016/j.vacuum.2020.109953.
50. T. Abe, Effect of short-range ordering in high-entropy alloys. *Mater. Trans.* **62**, 711–718 (2021), 10.2320/matertrans.MT-M2021022.
51. S. Chen *et al.*, Chemical-affinity disparity and exclusivity drive atomic segregation, short-range ordering, and cluster formation in high-entropy alloys. *Acta Mater.* **206**, 116638 (2021), 10.1016/j.actamat.2021.116638.
52. P. Singh *et al.*, Tuning phase stability and short-range order through Al doping in (CoCrFeMn)100–x A lx high-entropy alloys. *Phys. Rev. Mater.* **3**, 075002 (2019), 10.1103/PhysRevMaterials.3.075002.
53. F. Körmann, A. V. Ruban, M. H. F. Sluiter, Long-ranged interactions in bcc NbMoTaW high-entropy alloys. *Mater. Res. Lett.*, 10.1080/21663831.2016.1198837 (2017).
54. F. Otto, Y. Yang, H. Bei, E. P. George, Relative effects of enthalpy and entropy on the phase stability of equiatomic high-entropy alloys. *Acta Mater.* **61**, 2628–2638 (2013), 10.1016/j.actamat.2013.01.042.
55. G. Kresse, J. Furthmüller, Efficient iterative schemes for ab initio total-energy calculations using a plane-wave basis set. *Phys. Rev. B Condens. Matter Mater. Phys.* **54**, 11169–11186 (1996).
56. D. Kresse, G. Joubert, From ultrasoft pseudopotentials to the projector augmented-wave method. *Phys. Rev. B Condens. Matter Mater. Phys.* **59**, 1758–1775 (1999).
57. J. P. Perdew, K. Burke, M. Ernzerhof, Generalized gradient approximation made simple. *Phys. Rev. Lett.* **77**, 3865–3868 (1996).
58. H. J. Monkhorst, J. D. Pack, Special points for Brillouin-zone integrations. *Phys. Rev. B* **13**, 5188–5192 (1976).
59. J. M. Cowley, X-ray measurement of order in single crystals of Cu3Au. *J. Appl. Phys.* **21**, 24–30 (1950).